

Highlighting the research collaboration among the Department of Engineering at Aarhus University, the Mechanics of Slender Structures (MOSS) Lab and Physics Department at Boston University, and Aalto University.

#### Kirigami actuators

The Japanese art of kirigami inspires new ways of crafting complex shapes in thin materials for mechanical actuation. Exploring the fundamental principles of this art through careful tailoring of geometry and topology of cuts on thin elastic sheets, it is possible to design actuators that scale from paper down to atomically-thin 2D materials.

#### As featured in:



See Marcelo A. Dias,  
Douglas P. Holmes *et al.*,  
*Soft Matter*, 2017, **13**, 9087.



[rsc.li/soft-matter-journal](http://rsc.li/soft-matter-journal)

Registered charity number: 207890



## Kirigami actuators†

Marcelo A. Dias,<sup>a</sup> Michael P. McCarron,<sup>c</sup> Daniel Rayneau-Kirkhope,<sup>d</sup>  
 Paul Z. Hanakata,<sup>e</sup> David K. Campbell,<sup>e</sup> Harold S. Park<sup>c</sup> and Douglas P. Holmes<sup>\*c</sup>

Cite this: *Soft Matter*, 2017, 13, 9087

Received 22nd August 2017,  
 Accepted 14th September 2017

DOI: 10.1039/c7sm01693j

rsc.li/soft-matter-journal

**Thin elastic sheets bend easily and, if they are patterned with cuts, can deform in sophisticated ways. Here we show that carefully tuning the location and arrangement of cuts within thin sheets enables the design of mechanical actuators that scale down to atomically-thin 2D materials. We first show that by understanding the mechanics of a single non-propagating crack in a sheet, we can generate four fundamental forms of linear actuation: roll, pitch, yaw, and lift. Our analytical model shows that these deformations are only weakly dependent on thickness, which we confirm with experiments on centimeter-scale objects and molecular dynamics simulations of graphene and MoS<sub>2</sub> nanoscale sheets. We show how the interactions between non-propagating cracks can enable either lift or rotation, and we use a combination of experiments, theory, continuum computational analysis, and molecular dynamics simulations to provide mechanistic insights into the geometric and topological design of kirigami actuators.**

Deformations that bend a material without stretching involve a very low amount of stored elastic energy, and therefore present an opportunity to enable morphing at minimal energetic cost. The potential to exploit these energetically favorable and soft modes has recently emerged with kirigami-based thin sheets,<sup>1–4</sup> in which the introduction of cuts has been utilized to give unique structural properties and non-linear behavior, such as auxeticity,<sup>5–7</sup> significantly enhanced stretchability,<sup>8,9</sup> flexible electronic devices,<sup>10</sup> and topologically guided morphings.<sup>11–16</sup> In this work, we present a variety of kirigami actuators whose dynamical pattern formation is controllable. We develop a novel form of non-linear control–response relationship in kirigami

geometries through the conversion of the linear displacement imposed on the boundary of the thin sheet into a range of predictable motions.

The four fundamental modes depicted in Fig. 1, namely roll (rotation about the *x*-axis), pitch (rotation about the *y*-axis), yaw (rotation about the *z*-axis), and lift (the *z*-axis out-of-plane displacement), arise from linear actuation, and they may in principle be combined to generate any motion in 3D space. To demonstrate this design goal, we create three orthogonal rotations and a vertical out-of-plane displacement and show the mechanism for understanding how these emerge from the coupled behavior of individual cuts. We provide a theory that captures the main large-scale features in the mechanics of these structures, and demonstrate that similar actuators can be realized in suspended 2D materials, such as graphene and MoS<sub>2</sub>.<sup>17,18</sup> Moreover, full characterization of the out-of-plane displacement that occurs as a result of a single cut in a thin sheet allows us to derive a scaling law that shows a robust link between simulation and experiment on length scales ranging over six orders of magnitude. Because kirigami actuators are scale-invariant, our findings can be applied to tailor the microstructure and functionality of mechanical metamaterials across the technological spectrum of length scales ranging across the nanoscale (NEMS),<sup>17–20</sup> the microscale (MEMS),<sup>21–24</sup> and the macroscale.<sup>25–28</sup>

The complex behavior of kirigami actuators arises from functionalizing cracks in thin plates. In other words, when a material is thin enough, cracks under tension may cause the system to buckle before failure through crack propagation.<sup>29,30</sup> Therefore, a deeper understanding of the mechanics of a single non-propagating crack on thin sheets is needed. Let us consider a cut of length *b* centered with respect to the sheet's length *L* and width *w*, and parallel to the clamped edges of the sheet (Fig. 2a). The sheet thickness *h* is small, such that  $h \ll L \sim w$ . Applying a uniaxial extension  $\Delta$  perpendicular to the crack causes the sheet to buckle out-of-plane at a critical force  $F_c$ . The typical deflection size is given by a maximum amplitude  $\delta_0$  centered between the crack tips, and this shape decays back to nearly flat before reaching the clamped boundaries

<sup>a</sup> Department of Engineering, Aarhus University, Inge Lehmanns Gade 10, 8000 Aarhus C, Denmark. E-mail: madias@eng.au.dk

<sup>b</sup> Department of Physics and Astronomy, James Madison University, Harrisonburg, VA 22807, USA

<sup>c</sup> Department of Mechanical Engineering, Boston University, Boston, MA, 02215, USA. E-mail: dpholmes@bu.edu

<sup>d</sup> Department of Applied Physics, Aalto University, FI-00076 Espoo, Finland

<sup>e</sup> Department of Physics, Boston University, Boston, MA 02215, USA

† Electronic supplementary information (ESI) available. See DOI: 10.1039/c7sm01693j

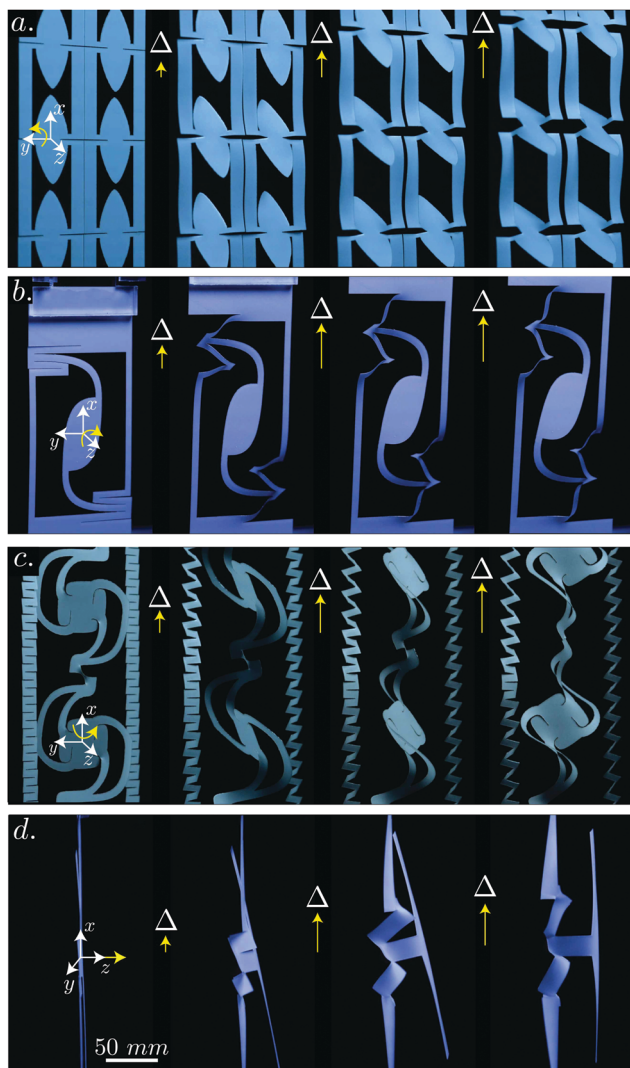


**Fig. 1** Examples of linear actuators from kirigami cut patterns. Extension, or applied displacement  $\Delta$ , along the  $x$ -direction causes (a) rotation about the  $y$ -axis or pitch, (b) rotation about the  $z$ -axis or yaw, (c) rotation about the  $x$ -axis or roll, and (d) out-of-plane deflection in the  $z$ -direction.

(Fig. 2b). This characteristic shape occurs on each side of the crack, such that the shape may be symmetric or antisymmetric about the plane aligned with the crack, normal to the initially flat surface—these two modes, respectively, correspond to stress intensity factors of bending and transverse shear.<sup>29,31</sup> We shall here focus our analysis on the symmetric kind, as the typical size of both out-of-plane deformations must be of the same order of magnitude. The critical force needed to trigger this instability is given by  $F_c$ , which depends on the ratio of the crack to sheet width,  $b/w$  (Fig. 2c). Since the instability results from an in-plane compressive zone (Fig. 2a) around the internal boundary along the crack,<sup>30,32</sup> this problem will be approximated by a beam of length  $b$ . Therefore,  $F_c$  is shown to collapse on a single curve (Fig. 2c) when the experimental data and simulation results are normalized by the characteristic buckling force  $Eh\Delta_c$ , where  $E$  is the Young's modulus of the material. This will become evident in eqn (5), where we derive  $\Delta_c \equiv h^2/b$

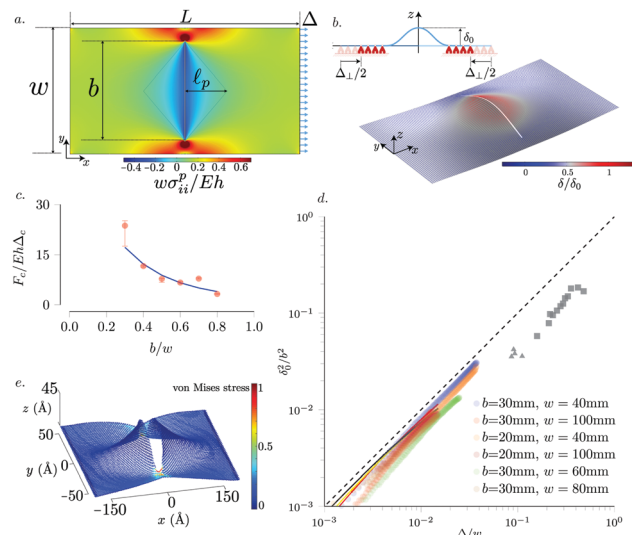


**Fig. 2** (a) Single cut's in-plane state of stress calculated by a Finite Element Method (FEM). Simulation parameters are set based on the experiments:  $h = 0.127$  mm,  $b = 80$  mm,  $w = 100$  mm,  $L = 182$  mm, Young's modulus  $E = 3.5$  GPa, Poisson's ratio  $\nu = 0.38$ , and  $\Delta \sim h$ . The color map shows the normalized sum of the principal stresses. (b) First mode of deformation where the color map represents the normalized deflection,  $\delta/\delta_0$ . (c) Critical force  $F_c$  required for buckling near the crack as a function of  $b/w$ . FEM simulation (solid lines) and experimental (disks with error bars) are shown. (d) Plot of  $\delta_0^2/b^2$  as a function of  $\Delta/w$  for experiments with mylar films (circles), FEM simulations (solid lines), and MD simulations of graphene (squares) and  $\text{MoS}_2$  (triangles). The scaling from eqn (5) is represented by the dashed line. Mylar and FEM parameters are set to  $h = 0.127$  mm,  $L = 182$  mm,  $E = 3.5$  GPa, and  $\nu = 0.38$ . MD simulations were done for a fixed  $L = 346$  Å, we plot data for width  $w = 114$  Å and cut lengths ranging from  $b = 38$  Å to  $76$  Å, and for  $w = 142$  Å with cuts ranging from  $b = 81$  Å to  $119$  Å. (e) A suspended graphene sheet ( $b = 76$  Å,  $w = 114$  Å,  $L = 346$  Å, and  $\Delta = 40$  Å), where the color map shows the von Mises stress scaled by its maximum value.

as the critical amount of in-plane compression at the buckling threshold.

To describe the post-buckled shape, we consider two regimes: the in-plane stretching dominated response to an applied extension  $\Delta$  normal to the single cut, and the out-of-plane state, where the buckling threshold is reached in the stress relief zone and the system becomes bending-dominated. This loading condition induces a crack opening mode described by the mode I stress intensity factor,  $K_I$ , which for a large plate in a state of uniform uniaxial stress is  $K_I = T\sqrt{\pi b/2}$ , where  $T$  is the tensile stress acting on the edge of the sheet.<sup>33</sup> From fracture mechanics,<sup>33</sup> it is established that the stress scales with the radius of curvature  $r$  of the cut:  $\sigma = K_I/\sqrt{2\pi r}$ . To estimate the tension in the sheet, we note that stresses concentrate near the crack and, in view of St. Venant's Principle,<sup>34</sup> it approaches an average value at a distance of about width  $w$  away from the crack. This approximation is also validated from the fact that beyond a sheet length to width ratio of about  $L/w \approx 1$ , the maximum deflection of the crack reaches a constant value indicating that, beyond a certain point, the sheet length does not contribute to the crack deformation. Therefore, we expect the tension in the sheet to scale as  $T \sim E\Delta/w$ . In our experiments, we take  $r \sim h$  for the crack radius. Therefore,

the stress in the sheet becomes  $\sigma \sim E(\Delta/w)(b/h)^{1/2}$ . The elastic strain energy due to stretching scales as  $\mathcal{U}_s \sim h(\sigma^2/E)A_s$ , where  $A_s = Lw$  is the area of the sheet, which reduces to

$$\mathcal{U}_s \sim E \frac{\Delta^2}{w} bL. \quad (1)$$

If we consider the sheet to be dominated by stretching, *i.e.* by initially neglecting the bending energy, the total potential energy is given as  $\mathcal{V} = \mathcal{U}_s - \mathcal{W}$ , where  $\mathcal{W}$  is the work done by the extension  $\Delta$ . Taking the work as the force  $(E\gamma^{(0)})A_s$  times the extension  $\Delta$ , where  $\gamma^{(0)}$  is the lateral strain of the sheet, and minimizing the total potential energy,  $(\partial/\partial\Delta)[E(\Delta^2/w)bL - E\gamma^{(0)}Lw\Delta] = 0$ , gives a relation for the lateral contraction,

$$\Delta_{\perp} \equiv \gamma^{(0)}w \sim b\Delta/w. \quad (2)$$

Note that eqn (2) is effectively a scaling of Poisson's contraction and sets up the base state for the in-plane solution. We now calculate the next-order contribution by allowing the stresses in the compressive zone to reduce the total energy through out-of-plane bending. The calculation is simplified by treating the problem as a 1D buckling of the free boundary along the crack (Fig. 2b), where both stretching and bending energies are required to provide the right balance. This next-order contribution is obtained as a minimizer of a dimensionally reduced model, along the arc-length  $s$  of the cut, given by

$$\mathcal{U} = \frac{bhE}{2} \int ds [\gamma^2 + h^2 \delta'^2], \quad (3)$$

where the new measure of strain is geometrically non-linear,  $\gamma \approx \gamma^{(0)} + \delta'^2/2$ , and  $\delta$  is the deflection. This yields a classic result for the maximum amplitude:

$$\delta_0 \sim \sqrt{b} \sqrt{\Delta_{\perp} - \Delta_c}, \quad (4)$$

where  $\Delta_c$  is related to the ratio between bending rigidity,  $B = h^3E$ , and stretching rigidity,  $Y = hE$ , as follows:  $\Delta_c/b \sim B/(b^2Y) = (h/b)^2$ . Inserting the in-plane compression result of eqn (2) into (4) gives a scaling for the maximum crack deflection,

$$\left(\frac{\delta_0}{b}\right)^2 \sim \frac{\Delta}{w} - \mathcal{O}\left(\frac{h}{b}\right)^2. \quad (5)$$

Eqn (5) shows a higher order dependency on the sheet thickness to crack length ratio, implying the invariance of these deformations from the macro- to nanoscale. To confirm this relationship, experiments were performed with single cuts in mylar films (biaxially-oriented polyethylene terephthalate—BoPET) to measure the maximum deflection as a function of extension for a given crack size and sheet width (see the ESI† for methods). Finite-Element Method (FEM) simulations with the same material parameters were also performed (see the ESI† for methods). Additionally, we carried out Molecular Dynamics (MD) simulations of suspended graphene monolayers (see the ESI† for methods). Fig. 2d shows the dimensionless deflection data for the experiments and simulations, along with the scaling prediction from eqn (5), confirming a very strong agreement across six orders of magnitude.

In order to generate simple actuators that can become the building blocks for more complex structures, such as mechanical

metamaterials, we must quantify how multiple cracks will interact to generate motion of points on the sheet. Since the behavior of a single crack is well described by eqn (5), the simplest extension is two parallel cracks of length  $b$  separated by distance  $\ell_s$ . When  $\ell_s/L$  is small, these cracks interact to generate vertical lift of the sheet between them (Fig. 3a-i and ii). However, the deflection of the center point of the sheet drops off quickly as the spacing between the cracks is increased, making it difficult to lift a large amount of surface area (Fig. 3b). Keeping  $\ell_s/L$  small while increasing the area of the sheet that is lifted can be accomplished by extending a portion of each crack towards the clamped boundaries (Fig. 3a-iii). This relies on the same buckling mechanism that governs the single crack behavior, producing nearly the same amount of lift as the two parallel cracks (Fig. 3c). These additional cuts also introduce wrinkles on the sheet, which can be avoided by introducing cuts that provide room for the in-plane compression (Fig. 3a-iv). With this arrangement of cuts, we demonstrate how these parallel cracks can become building blocks for generating lift of a large localized area.

We note that the four crack tips of the two parallel cracks in Fig. 3a-i form a rectangular unit cell (convex polygon) and generate lift in the sheet. This rudimentary shape is identified quantitatively by following the lines of tension that connect two neighboring cracks, and the convexity of the unit cell signifies how much stretching within the sheet can be transferred into a crack opening displacement. Convex shapes constrain the sheet to induce vertical lift, while concave shapes have the freedom to rotate. To illustrate this idea, we focus on the pitch mode. We performed a post-buckling analysis through FEM simulations for the geometry in Fig. 4a, while varying the crack length  $L_c$ , thus allowing us to scan unit cell shapes from convex to concave. Denoting  $L_{\parallel}$  as the cut length parallel to the clamped boundary, we refer to the ratio  $(2L_c + L_{\parallel})/w$  as a measure of convexity. The target shape strongly depends on

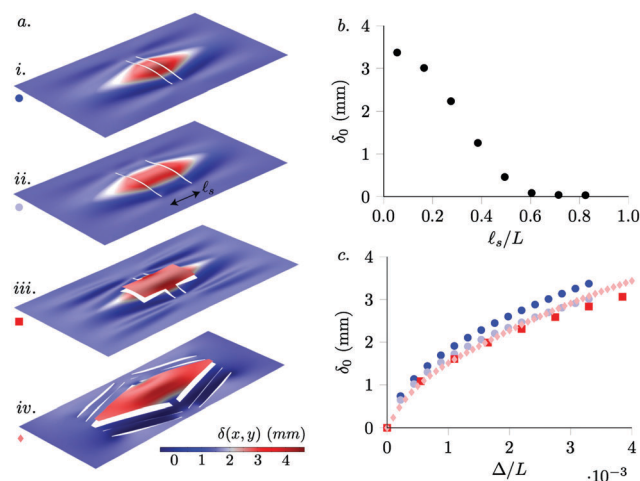
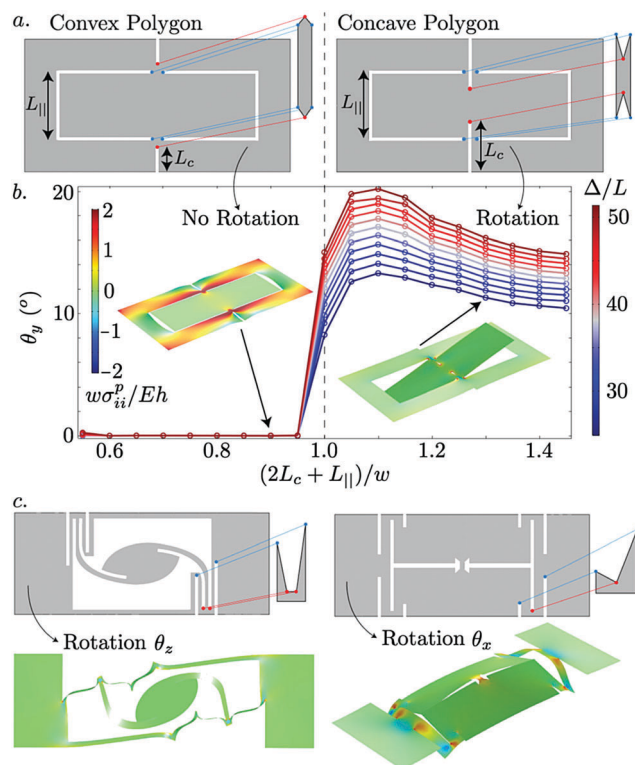


Fig. 3 (a) FEM simulations using two cuts as the basis for generating lift. (b) Increasing the spacing between two cuts causes the lift of the center of the sheet to significantly drop. (c) By using additional cuts in (iii) and (iv), we can generate the same lift as with (ii) while lifting a much larger area.



**Fig. 4** (a) Schematics illustrating how the polygon formed by crack tips will generate rotation. (b) As the polygon formed by the edge crack tip and the internal crack tips changes from convex to concave, we can see the emergence of rotation about the  $y$ -axis. (c) The coupling of multiple concave polygons formed by the crack tips can enable rotation about the  $x$ - or  $z$ -axis as well.

this parameter's transition: lift of the outer portion of the sheet occurs when the unit cell is convex, *i.e.*  $(2L_c + L_{\parallel})/w < 1$ , while rotation about the  $y$ -axis occurs when it is concave, *i.e.*  $(2L_c + L_{\parallel})/w \gtrsim 1$  (Fig. 4b). Generating rotation about the  $z$  and  $x$  axes follows the same principle—concave unit cells enable rotation (Fig. 4c). In these more complex configurations, there is coupling between two unit cells within the sheet. While an intricate model of the coupling between multiple unit cells is beyond the scope of this work, it is clear from the schematics and post-buckled shapes that the concave unit cells locally enable rotation about the  $z$  and  $x$  axes.

Fig. 4 indicates that the convexity of the unit cell formed by the locally interacting crack tips can generate either lift or rotation. We provide further insight through quantifying the magnitude of these kirigami-based motions by measuring the lift or rotation as a function of relative strain  $\Delta/L$  (Fig. 5). Here we show that a portion of the sheet can be lifted vertically by an amount nearly 50 times the sheet thickness. Since there is no plastic deformation and the cracks do not propagate, these deformations are reversible. The stiffness of the sheets designed to provide rotation varies widely. Rotations about the  $y$  (pitch) and  $x$  (roll) axes reach about 60 degrees after a moderate amount of extension, while the in-plane rotation about the  $z$ -axis requires a significant amount of extension to reach 30 degrees of rotation. Fig. 5a shows good agreement

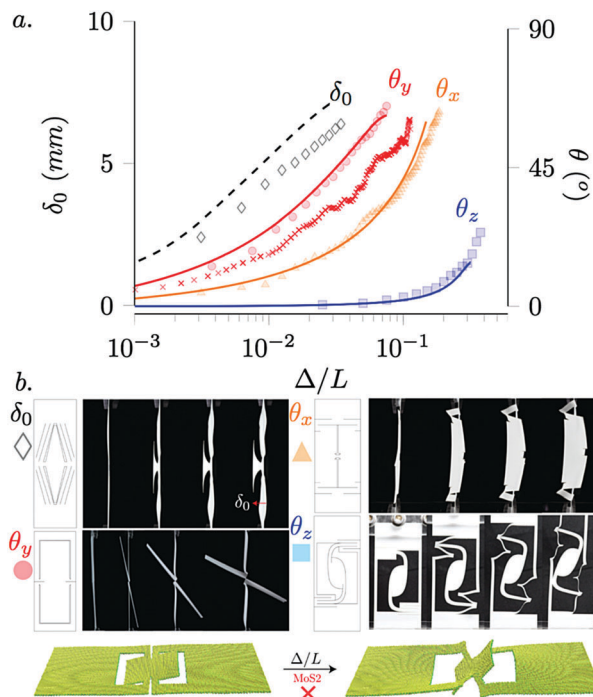


**Fig. 5** (a) A plot of the lift of the center  $\delta_0$  (black) and the three rotations as functions of  $\Delta/L$ ,  $\Delta$  being the applied displacement in the  $x$ -direction. The experimental data are represented by black diamonds for the lift, orange triangles for the roll (rotation about the  $x$ -axis), red disks for the pitch (rotation about the  $y$ -axis), and blue squares for the yaw (rotation about the  $z$ -axis). FEM for the respective modes of deformation, using the same parameters of the experiments, are shown in dashed and solid curves. The red  $x$ 's show the results of the molecular dynamics simulations. (b) Images of the experiments for the cut patterns and the sequence of deformation as  $\Delta/L$  is increased as well as two snapshots of the molecular dynamics simulation. In the case of  $\text{MoS}_2$ , the geometric parameters are: length  $L = 460 \text{ \AA}$  and width  $w = 152 \text{ \AA}$  of the sheet; crack length  $L_c = 47.5 \text{ \AA}$ ; and a  $240 \text{ \AA}$  length and a  $82 \text{ \AA}$  width ( $L_{\parallel}$ ) of the inner rotating ribbon.

between the experimental measurements for the macroscale designs of lift (diamonds for  $\delta_0$ ) and rotation (triangles for  $\theta_x$ , disks for  $\theta_y$ , and squares for  $\theta_z$ ) and the FEM simulations (dashed line for  $\delta_0$ , orange for  $\theta_x$ , red for  $\theta_y$ , and blue for  $\theta_z$ ).

The results from Fig. 2d suggest that these actuator designs should scale down to 2D materials. From a  $\text{MoS}_2$  monolayer, we tested the simplest nanoactuator requiring only one unit cell for rotation about the  $y$ -axis, *i.e.* the pitch mode shown at the bottom in Fig. 5b. We obtained a rigid rotation due to its higher bending modulus than that of graphene.<sup>35</sup> We applied an extension perpendicular to the crack and measured the rotation of the inner ribbon about the  $y$ -axis (Fig. 5a, red  $x$ 's). At small  $\Delta/L$ , there is good agreement between the macroscale results and the nanoscale simulations, and eventually the three actuators achieve nearly the same maximum value of  $\theta_y$ . While the behavior is qualitatively similar across several orders of magnitude in sheet thickness, it is clear that the agreement for the 2D kirigami is qualitative rather than quantitative. Specifically, the fact that the rotation that is observed in the 2D kirigami is smaller for the same strains than the bulk system suggests that the 2D system may undergo more stretching than the bulk system, a point also made

recently by Grosso and Mele.<sup>36</sup> Therefore, additional analysis of the 2D material kirigami actuators is necessary to quantitatively replicate the macroscale actuator designs.

Finally, we return to the actuators in Fig. 1. Through replicating the mechanism in Fig. 4a, we can see the rotation about the  $y$ -axis of all cells (Fig. 1a). This indicates that building blocks can go beyond mechanism design towards the development of mechanical metamaterials. Furthermore, the interactions between multiple cuts can enable portions of a thin sheet to rotate one complete revolution about the  $x$ -axis, the extension axis (Fig. 1c), while coupling unit cells that cause rotation and lift generate sheets that first rotate about the  $y$ -axis and subsequently lift in the  $z$  direction (Fig. 1d). What remains is to better understand how building blocks can be combined to generate targeted behaviors—an inverse problem that can we can begin to approach by considering the simple geometric model we present here.

We have addressed two fundamental problems that are pivotal to connecting kirigami actuators to practical designs for engineering applications: scale-invariant behavior and a robust geometric mechanism for actuator design. While the kirigami mechanics has been unified over six orders of magnitude in sheet thickness, the shape of a unit cell formed by locally interacting crack tips provides a geometric mechanism to induce either lift or rotation. What we present has the potential to offer rational design tools for dynamical assembling of complex geometries,<sup>10,28</sup> and we hope that this spontaneous generation of shapes emerging from quasi-static actuation comes to complement inverse design algorithms that have been proposed for lattice-based kirigami.<sup>14,15</sup> As previously mentioned, the cracks do not propagate in the experiments performed here, thus the process remains entirely reversible. In order to maintain this reversibility in systems utilizing materials with lower yield stress, cracks can be made with a larger crack tip radius  $r$ , thus lowering the stress intensity factor,  $K_I$ . The scaling found here is robust under such a modification since a few multiples of  $r$  only yield a pre-factor in front of eqn (5), thus preserving the same power-law. It should also be noted that the propagation of interacting cracks can be manipulated by their initial geometry,<sup>37,38</sup> such interactions could be utilized to increase the functionality of the kirigami structures and/or give a predictable response to strain beyond that which causes crack propagation. There may also be significant scientific benefits to demonstrating kirigami actuation in 2D materials. From a basic science perspective, kirigami provides an ideal platform to study the localization of electronic states or the coupling of 2D quantum dots.<sup>39</sup> Alternatively, these structures offer significant opportunities for flexible, lightweight band-gap engineered optoelectronic materials whose performance can be reversibly changed and manipulated over a wide range of the optical spectrum by locally varying the strain.<sup>40–47</sup>

## Author contributions

M. A. D. and D. P. H. conceived the study and proposed the research; M. A. D. and D. R. K. performed the mathematical modeling and FEM in consultation with D. P. H.; M. P. M. and

D. P. H. performed the experiments in consultation with M. A. D.; P. Z. H., D. K. C., and H. S. P. performed the molecular simulation studies; M. A. D. and D. P. H. wrote the main article; and all authors jointly edited the entire article.

## Conflicts of interest

The authors declare no conflict of interest.

## Acknowledgements

M. A. D. is grateful to M. Adda-Bedia, J. Bico, B. Roman, and K. Seffen for many insightful discussions. M. A. D. would also like to thank ENS-Lyon and ESPCI-Paris for hosting the author during part of the development of this manuscript and funding from the 4-VA program for collaborative research at JMU. D. P. H. is grateful to the National Science Foundation (CMMI CAREER-1454153) for financial support. M. A. D., D. R. K., and D. P. H. would like to thank I. Metta for useful discussions at the start of this project. D. K. C. acknowledges the Aspen Center for Physics, which is supported by the National Science Foundation grant PHY-1607611, where part of this work was completed. D. R. K. acknowledges funding from Academy of Finland.

## References

- 1 P. M. Reis, *J. Appl. Mech.*, 2015, **82**, 111001.
- 2 K. A. Seffen, *Phys. Rev. E*, 2016, **94**, 033003.
- 3 A. Rafsanjani and K. Bertoldi, *Phys. Rev. Lett.*, 2017, **118**, 084301.
- 4 J. Bico, E. Lepoivre, H. Bense, E. Reyssat and B. Roman, *Bull. Am. Phys. Soc.*, 2017, **62**.
- 5 K. Virk, A. Monti, T. Trehard, M. Marsh, K. Hazra, K. Boba, C. D. L. Remillat, F. Scarpa and I. R. Farrow, *Smart Mater. Struct.*, 2013, **22**, 084014.
- 6 F. Scarpa, M. Ouisse, M. Collet and K. Saito, *Journal of Vibration and Acoustics*, 2013, **135**, 041001.
- 7 Y. Tang and J. Yin, *Extreme Mechanics Letters*, 2017, **12**, 77–85.
- 8 T. C. Shyu, P. F. Damasceno, P. M. Dodd, A. Lamoureux, L. Xu, M. Shlian, M. Shtein, S. C. Glotzer and N. A. Kotov, *Nat. Mater.*, 2015, **14**, 785–789.
- 9 N. Vachicouras, C. M. Tringides, P. B. Campiche and S. P. Lacour, *Extreme Mechanics Letters*, 2017, **15**, 63–69.
- 10 Y. Zhang, Z. Yan, K. Nan, D. Xiao, Y. Liu, H. Luan, H. Fu, X. Wang, Q. Yang, J. Wang, W. Ren, H. Si, F. Liu, L. Yang, H. Li, J. Wang, X. Guo, H. Luo, L. Wang, Y. Huang and J. A. Rogers, *Proc. Natl. Acad. Sci. U. S. A.*, 2015, **112**, 11757–11764.
- 11 J.-F. Sadoc, N. Rivier and J. Charvolin, *Acta Crystallogr., Sect. A: Found. Crystallogr.*, 2012, **68**, 470–483.
- 12 J. Charvolin and J.-F. Sadoc, *Biophys. Rev. Lett.*, 2011, **6**, 13–27.
- 13 J.-F. Sadoc, J. Charvolin and N. Rivier, *J. Phys. A: Math. Theor.*, 2013, **46**, 295202.
- 14 T. Castle, Y. Cho, X. Gong, E. Jung, D. M. Sussman, S. Yang and R. D. Kamien, *Phys. Rev. Lett.*, 2014, **113**, 1–5.

- 15 D. M. Sussman, Y. Cho, T. Castle, X. Gong, E. Jung, S. Yang and R. D. Kamien, *Proc. Natl. Acad. Sci. U. S. A.*, 2015, **201506048**.
- 16 B. G.-G. Chen, B. Liu, A. A. Evans, J. Paulose, I. Cohen, V. Vitelli and C. D. Santangelo, *Phys. Rev. Lett.*, 2016, **116**, 135501.
- 17 Z. Qi, D. K. Campbell and H. S. Park, *Phys. Rev. B*, 2014, **90**, 245437.
- 18 M. K. Blees, A. W. Barnard, P. A. Rose, S. P. Roberts, K. L. McGill, P. Y. Huang, A. R. Ruyack, J. W. Kevek, B. Kobrin, D. A. Muller and P. L. McEuen, *Nature*, 2015, **524**, 204–207.
- 19 K. Cai, J. Luo, Y. Ling, J. Wan and Q.-H. Qin, *Sci. Rep.*, 2016, **6**, 35157.
- 20 T. Han, F. Scarpa and N. L. Allan, *Thin Solid Films*, 2017, **632**, 35–43.
- 21 Z. Song, X. Wang, C. Lv, Y. An, M. Liang, T. Ma, D. He, Y.-J. Zheng, S.-Q. Huang, H. Yu and H. Jiang, *Sci. Rep.*, 2015, **5**, 10988.
- 22 L. Xu, X. Wang, Y. Kim, T. C. Shyu, J. Lyu and N. A. Kotov, *ACS Nano*, 2016, **10**, 6156–6162.
- 23 J. Rogers, Y. Huang, O. G. Schmidt and D. H. Gracias, *MRS Bull.*, 2016, **41**, 123–129.
- 24 A. Baldwin and E. Meng, Micro Electro Mechanical Systems (MEMS), 2017 IEEE 30th International Conference on, 2017, pp. 227–230.
- 25 K. Saito, F. Agnese and F. Scarpa, *J. Intell. Mater. Syst. Struct.*, 2011, **22**, 935–944.
- 26 S. Sareh and J. Rossiter, *Smart Mater. Struct.*, 2012, **22**, 014004.
- 27 K. Zhang and J. S. Dai, *Journal of Mechanisms and Robotics*, 2014, **6**, 021007.
- 28 A. Lamoureux, K. Lee, M. Shlian, S. R. Forrest and M. Shtein, *Nat. Commun.*, 2015, **6**, 8092.
- 29 C. Y. Hui, A. T. Zehnder and Y. K. Potdar, *Int. J. Fract. Mech.*, 1998, **93**, 409–429.
- 30 R. Brighenti, *Thin-Walled Structures*, 2005, **43**, 209–224.
- 31 A. T. Zehnder and M. J. Viz, *Appl. Mech. Rev.*, 2005, **58**, 37.
- 32 M. Adda-Bedia and M. Ben Amar, *Phys. Rev. Lett.*, 2001, **86**, 5703.
- 33 Z. P. Bazant and L. Cedolin, *Stability of Structures: Elastic, Inelastic, Fracture and Damage Theories*, World Scientific, 2010.
- 34 N. I. Muskhelishvili, *Some Basic Problems of the Mathematical Theory of Elasticity*, Springer, Netherlands, 2013.
- 35 J.-W. Jiang, Z. Qi, H. S. Park and T. Rabczuk, *Nanotechnology*, 2013, **24**, 435705.
- 36 B. F. Grosso and E. J. Mele, *Phys. Rev. Lett.*, 2015, **115**, 195501.
- 37 P.-P. Cortet, G. Huillard, L. Vanel and S. Ciliberto, *J. Stat. Mech.: Theory Exp.*, 2008, **2008**, P10022.
- 38 M.-J. Dalbe, J. Koivisto, L. Vanel, A. Miksic, O. Ramos, M. Alava and S. Santucci, *Phys. Rev. Lett.*, 2015, **114**, 205501.
- 39 D. A. Bahamon, Z. Qi, H. S. Park, V. M. Pereira and D. K. Campbell, *Phys. Rev. B*, 2016, **93**, 235408.
- 40 A. Castellanos-Gomez, R. Roldán, E. Cappelluti, M. Buscema, F. Guinea, H. S. van der Zant and G. A. Steele, *Nano Lett.*, 2013, **13**, 5361–5366.
- 41 M.-Y. Tsai, A. Tarasov, Z. R. Hesabi, H. Taghinejad, P. M. Campbell, C. A. Joiner, A. Adibi and E. M. Vogel, *ACS Appl. Mater. Interfaces*, 2015, **7**, 12850–12855.
- 42 K. He, C. Poole, K. F. Mak and J. Shan, *Nano Lett.*, 2013, **13**, 2931–2936.
- 43 D. Lloyd, X. Liu, J. W. Christopher, L. Cantley, A. Wadehra, B. L. Kim, B. B. Goldberg, A. K. Swan and J. S. Bunch, *Nano Lett.*, 2016, **16**, 5836–5841.
- 44 J. Feng, X. Qian, C.-W. Huang and J. Li, *Nat. Photonics*, 2012, **6**, 866–872.
- 45 H. J. Conley, B. Wang, J. I. Ziegler, R. F. Haglund Jr, S. T. Pantelides and K. I. Bolotin, *Nano Lett.*, 2013, **13**, 3626–3630.
- 46 P. Johari and V. B. Shenoy, *ACS Nano*, 2012, **6**, 5449–5456.
- 47 V. N. Kotov, B. Uchoa, V. M. Pereira, F. Guinea and A. C. Neto, *Rev. Mod. Phys.*, 2012, **84**, 1067.